Journal of Nuclear Materials 400 (2010) 157–174

Contents lists available at ScienceDirect

Journal of Nuclear Materials

journal homepage: www.elsevier.com/locate/jnucmat

Mechanical behaviors of the dispersion nuclear fuel plates induced by fuel particle swelling and thermal effect I: Effects of variations of the fuel particle volume fractions

Qiming Wang, Xiaoqing Yan, Shurong Ding *, Yongzhong Huo

Department of Mechanics and Engineering Science, Fudan University, Shanghai 200433, China

ARTICLE INFO

Article history:
Received 20 August 2009
Accepted 1 March 2010

ABSTRACT

A new method of modeling the in-pile mechanical behaviors of dispersion nuclear fuel elements is proposed. Considering the irradiation swelling together with the thermal effect, numerical simulations of the in-pile mechanical behaviors are performed with the developed finite element models for different fuel particle volume fractions of the fuel meat. The effects of the particle volume fractions on the mechanical performances of the fuel element are studied. The research results indicate that: (1) the maximum Mises stresses and equivalent plastic strains at the matrix increase with the particle volume fractions at each burnup; the locations of the maximum first principal stresses shift with increasing burnup; at low burnups, the maximum first principal stresses increase with the particle volume fractions; while at high burnups, the 20% volume fraction case holds the lowest value; (2) at the cladding, the maximum equivalent plastic strains and the tensile principal stresses increase with the particle volume fractions; while the maximum Mises stresses do not follow this order at high burnups; (3) the maximum Mises stresses at the fuel particles increase with the particle volume fractions, and the particles will engender plastic strains until the particle volume fraction reaches high enough.

1. Introduction

The dispersion nuclear fuel elements have been widely used in the research and test reactors since the Reduced Enrichment for Research and Test Reactors (RERTR) program started in 1970s. This program has been tasked with the conversion of research reactors from high-enriched uranium (HEU) to low-enriched uranium (LEU) with a U^{235} content of less than 20%. These reactors could be used as a neutron source with high thermal neutron flux density for experimental purposes. In order to reach the requisite power density of the fuel element with low-enriched uranium, the needs to raise the density of the existing fuels should be met. Owing to the high uranium density of dispersion nuclear elements [1,2], several kinds of dispersion fuels such as the U_3Si_2 dispersion fuel are formally qualified for reactor use and a good many research and test reactors have been converted to LEU fuels. A number of irradiation tests [3–6] are being carried out in order to improve further the performances of the current dispersion fuel elements.

The dispersion fuel elements (DFEs) have very complex in-pile thermal and mechanical behaviors. Nuclear fissions of the fuel particles attacked by the neutrons in the nuclear reactor produce fission heat along with the solid and inert gas fission products. For one thing, the fission products can lead to volume swelling of the fuel particles with increasing burnup and the configuration of the fuel element will be updated accordingly; for another, the fission gas would migrate to the free volumes with rise of burnup, and would form the bubble nucleus if caught by flaws, dislocation, and cavity on the grain boundary, then the bubble nucleus would grow with absorption of the liberated fission gas [7]. The nuclear experiment [8] showed that the in-pile thermal–mechanical performance of the dispersion fuel element was intensely affected by the fuel volume fractions.

Since the irradiation experimental research is very time-consuming and the in-pile behaviors found in the experiment [9] need to be interpreted, a numerical simulation is becoming an important approach to explain the experiment results and carry out the optimal design. Recently, the relative researches on the dispersion fuel plate with the finite element method (FEM) appeared and some specific codes for the thermal and thermal–mechanical analysis were developed and were being upgraded, including FASTDART [10,11], PLATE [12,13], MAIA [14,15] and DART-TM [16] and so on. In these studies, the dispersion fuel meat was generally treated as homogeneous and the modeling was two-dimensional, that is, the mutual actions between the fuel particles and the matrix, and the mutual actions among fuel particles are not taken into

* Corresponding author.
E-mail address: dsr1971@163.com (S. Ding).

0022-3115/$ - see front matter © 2010 Elsevier B.V. All rights reserved.
doi:10.1016/j.jnucmat.2010.03.003

account. Böning [17] simulated the irradiation swelling of the full-sized U_3Si_2–Al fuel plate, whose meat was regarded as a homogeneous one, revealing that the dispersion fuel plate with the particle volume fraction being about 20% had presented a remarkable swelling ratio under the studied irradiation condition. Van Duyn [2] studied the PuO_2–Zr dispersion rod-like fuel element with FEM, taking account of the distribution of the fuel particles more accurately, while the simulation was relatively simple. Shurong Ding et al. [18,19] studied the thermal and mechanical behaviors in the plate-type dispersion nuclear fuel element, but they did not draw the actual cladding structure into consideration and the temperature field with increasing burnup is supposed to be the same as the one induced by the thermal effect. Above all, the numerical-simulation study of the effects of the micro-structures of dispersion fuel elements on the in-pile mechanical behaviors is limited.

In this study, in accordance with the micro-constructions of plate-type dispersion nuclear fuel elements, the three-dimensional finite element models are developed respectively for different particle volume fractions of the fuel meat, which might simulate not only the micro stress–strain field but also the macro deformation along the thickness. A new method of modeling the in-pile mechanical behaviors is proposed. In order to investigate the in-pile mechanical behaviors and carry out optimal design, numerical simulations of the in-pile mechanical behaviors induced by the irradiation swelling together with the thermal effects are performed. And the effects of variations of the fuel particle volume fractions (10%, 20% and 30%) of the fuel meat on the in-pile mechanical behaviors are studied.

2. Basic formula and relations

This study is conducted on one kind of typical dispersion fuel element, having an alloy cladding and a meat with the fuel particles being dispersively embedded in a metal matrix. Owing to easy acquirements of the material parameters of uranium dioxide (UO_2) and zircaloy, UO_2 and zircaloy are set as the materials of the fuel particles and the metal matrix (and the cladding), respectively.

Since the fission heat and the updated configuration induced mainly by the fuel swelling would lead to variations of the temperature field, the in-pile mechanical behaviors of the fuel element might be remarkably affected due to the temperature-dependence of the material parameters. In order to determine the stress–strain field, the temperature field should be calculated first. Thus, the whole burnup can be divided into lots of time steps, and at every time step, the temperature field can be regarded as a steady-state one. With the temperature field at every time step determined, the relative mechanical fields can be calculated subsequently. It can be called a thermal–mechanical coupling analysis problem. In this section, the basic equations and the required material parameters are given.

2.1. Heat conduction analysis model

For steady-state thermal problems, the temperature distributions of fuel elements are influenced by the thermal conductivities of the fuel particles and matrix, the fission rates of the fuel particles and the heat transfer coefficient between the cladding and the coolant water. So, the temperature-related material properties will be given.

2.1.1. The heat generation rate of the fuel particles

The heat generation rate of the fuel particles is obtained as

$$\dot{q} = c \cdot \dot{f} \tag{1}$$

where $c = 3.204 \times 10^{-11}$ J/fission is the generated heat energy by every fission event and $\dot{f}$ is the fission rate of the fuel particles.

2.1.2. Thermal conductivities of fuel particles

The model of thermal conductivities of fuel particles improved by Lucuta et al. [20] consists of five contributions and can be expressed as

$$K_{UO_2} = K_0 \cdot FD \cdot FP \cdot FM \cdot FR \tag{2}$$

where K_0 is Harding's expression for the thermal conductivity of unirradiated UO_2; *FD* quantifies the effect of dissolved fission products; *FP* describes the effect of precipitated solid fission products; *FM* is the modified Maxwell factor for the effect of the pore and fission-gas bubbles; *FR* characterizes the effect of radiation damage.

2.1.3. Thermal conductivities of matrix and cladding

For the zircaloy matrix and cladding, its thermal conductivity from the room temperature to the melting point can be expressed by [21]:

$$k = 7.51 + 2.09 \times 10^{-2}T - 1.45 \times 10^{-5}T^2 + 7.67 \times 10^{-9}T^3 \tag{3}$$

where T (K) denotes the temperature in Kelvin.

2.2. The constitutive model of fuel particles

The thermal expansion of UO_2 fuel particles relative to 300 K can be expressed as [22]

$$\Delta l/l_0 = -3.0289 \times 10^{-4} + 8.4217 \times 10^{-6}(T - 273) + 2.1481 \times 10^{-9}(T - 273)^2 \tag{4}$$

where T (K) denotes the temperature with the application range from 300 K to 1530 K.

The elastic modulus of UO_2 fuel particles can be described as [23]

$$E = 2.26 \times 10^{11}[1 - 1.131 \times 10^{-4}(T - 273.15)][1 - 2.62(1 - D)] \tag{5}$$

where E is the elastic modulus in Pa. T is the temperature in Kelvin and D is the theoretical density (92–98%). In addition, Poisson ratio v is set as 0.316.

The Misses hardening rule of UO_2 fuel particles is as the following [18]

$$\bar{\sigma} = \begin{cases} 66.9 - 0.0397T + (520.0 - 0.0386T)\bar{\varepsilon}_p & T \leqslant 1200^\circ C \\ 36.6 - 0.0144T + (139.5 - 0.0688T)\bar{\varepsilon}_p & T > 1200^\circ C \end{cases} \tag{6}$$

where $\bar{\sigma}$ is the Misses equivalent stress, whose unit is kg/mm^2; $\bar{\varepsilon}_p$ is the equivalent plastic strain.

The total swelling of the fuel particles include three parts: gas-bubble swelling, solid fission product swelling and the densification due to the variation of the porosity [22–24].

$$\left(\frac{\Delta V}{V}\right)^{gs} = 439.6 \exp\left(-\frac{16,450}{T - 100}\right) \tag{7}$$

$$\left(\frac{\Delta V}{V}\right)^{ss} = 0.0025 \tag{8}$$

The above two expressions depict the volume variations due to gas-bubble swelling and solid fission product swelling per 10^{20} fissions/cm^3 T is the temperature in Kelvin.

$$\left(\frac{\Delta V}{V}\right)^{ds} = \{0.0142[1 - \exp(-6.7943BU)] + 0.00893[1 - \exp(-1.1434BU)]\} \cdot ADST \tag{9}$$

Expression (10) depicts densification of UO_2, where *BU*: burn-up (*MWD*/kgUO_2), *ADST*: adjusting factor (=0.6).

2.3. The material model of the matrix and cladding

The matrix and cladding adopt the same material Zircaloy. The thermal expansion coefficient [21] is 5.58×10^{-6}/K. The Young's modulus and Poisson's ratio introduce Fisher Model [25]:

$$E = 9.9 \times 10^5 - 566.9 \times (T - 273.15) \times 9.8067 \times 10^4 \quad (10)$$

$$v = 0.3303 + 8.376 \times 10^{-5}(T - 273.15) \quad (11)$$

where E is Young's modulus in Pa, T is temperature in Kelvin and v is Poisson's ratio.

The strain-hardening curve is described as [26]:

$$\sigma = K\varepsilon^n \cdot \left(\frac{\dot{\varepsilon}}{10^{-3}}\right)^m \quad (12)$$

where σ is the true stress, ε is the true strain, n is the strain-hardening exponent, K is strength coefficient and m is strain rate sensitivity exponent. $\dot{\varepsilon}$ is true strain rate. If $\dot{\varepsilon} < 10^{-5}/s$, set $\dot{\varepsilon} = 10^{-5}/s$.

$$K = 1.0884 \times 10^9 - 1.0571 \times 10^6 T \quad (13)$$

$$n = -1.86 \times 10^{-2} + T(7.11 \times 10^{-4} - 7.721 \times 10^{-7} T) \quad (14)$$

$$m = 0.02 \quad (15)$$

where T is the temperature in Kelvin with the application range from 300 K to 730 K.

3. The finite element model

3.1. Selection of the Representative Volume Element and the finite element model

Similar to the modeling method of our previous work [19], the Representative Volume Element (RVE) as shown in Fig. 1 can be selected with assuming that the fuel particles are periodically distributed along the length and width directions. For example, with the assumption that the spherical particles are cubically arranged in the matrix illustrated as Fig. 2a, according to the periodicity and the actual geometry shape that the sizes along the length direction and the width direction are much larger than the one along the thickness, the RVE is selected as Fig. 2b. For the sake of calculation efficiency, the finite element model is selected according to the symmetry of the RVE to be 1/8 fraction of the RVE, shown as Fig. 2c. The plane $Z = 0$ expresses the mid-plane of the fuel plate and the plane with $Z = H/2$ denotes the upside surface which is the contact surface with the coolant water.

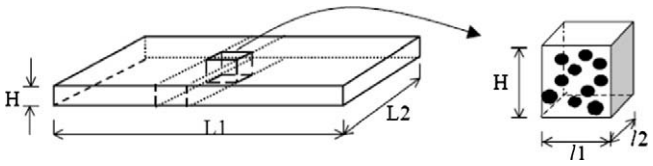

Fig. 1. Dispersion fuel plate and the Representative Volume Element.

In this study, the meat thickness is set as 1.27 mm and the cladding thickness maintains 0.4 mm. The finite element models are developed respectively for different particle volume fractions (10%, 20% and 30%) of the fuel meat, with the particle diameter $d = 100$ μm and with the same simple cubic distribution form, as shown in Fig. 3, supposing that the bonding of the fuel particles and the metal matrix, and the one of the cladding and the fuel meat are perfect.

3.2. Mesh grid for the respective finite element models

The thermal–mechanical coupling element C3D8RT in the commercial software ABAQUS is used to discretize the finite element models. The mesh grids, the node and element information of the developed finite element models are presented in Fig. 3 and Table 1. Convergence of the computing result is investigated through checking the trend of the calculated result as a function of mesh size. The final meshes are determined according to the convergence investigation in the meshes, therefore the obtained results in this study have been testified to have enough precision.

3.3. Boundary conditions

Since the mechanical analysis in this work is coupled with the thermal analysis, two sets of boundary conditions should be taken into account at the same time. The boundary conditions to determine the temperature field are given as

(1) Except the upside surface $Z = H/2$, the other surfaces of the finite element models all satisfy: $-k\frac{\partial T}{\partial n} = 0$.
(2) The upside surface $Z = H/2$ satisfy the convective boundary condition: $-k\frac{\partial T}{\partial n} = h(T - T_f)$, where the temperature of the periphery fluid T_f is 573 K and the heat transfer coefficient used is 2×10^{-2} W/mm^2 K.

The used boundary conditions to determine the structural fields are as the following:

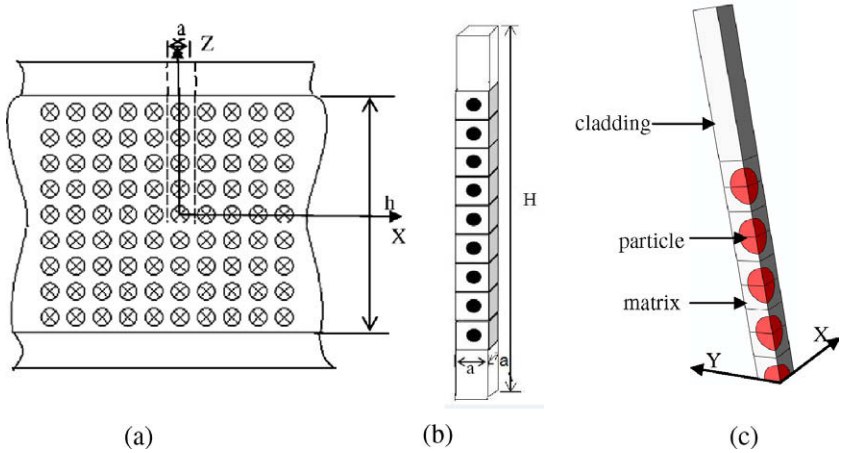

Fig. 2. (a) The sketch map, (b) RVE and (c) finite element model of the dispersion fuel plate.

Fig. 3. Finite element models for different particle volume fractions: (a) 10%, (b) 20%, and (c) 30%.

Table 1
Element information for finite element models with different volume fractions.

Volume fraction (%)	Element pattern	Number of elements	Number of nodes
10	C3D8RT	18,155	21,334
20	C3D8RT	23,448	27,727
30	C3D8RT	28,515	32,847

(1) The symmetric boundary condition is applied at all the surfaces of the finite element models, except the upside surface $Z = H/2$.
(2) The continuous displacement conditions are met at the interfaces between the fuel particles and the matrix and the ones between the meat and the cladding.

4. Results and discussions

4.1. A simulation method of the in-pile behaviors

At the initial stage of burnup, the mechanical behavior is mainly induced by the temperature difference between the steady-state one and the room one. And with increasing burnup, the irradiation swelling is the main factor to result in variations of the mechanical behaviors. Thus, the total burnup can be divided into two stages: the initial stage of burnup and the increasing stage of burnup. And the total calculation is divided into two analysis steps.

The first analysis step is to model the mechanical behaviors at the initial stage of burnup. Firstly, the steady-state temperature field is solved, and then the displacement field, the strain field and the thermal stress field resulting from the temperature differences are calculated with the thermal–elastoplasticity method. In ABAQUS, the thermal–mechanical coupling element C3D8RT is chosen, the thermal and thermal–mechanical behaviors can be solved directly.

For the second analysis step, the irradiation-swelling simulation with increasing burnup becomes a key problem. The complexity exists in that: (1) the particle swelling will lead to appearance of large strains in the metal matrix and variation of the configuration of the fuel plate; (2) the changed configuration will bring the temperature variations within the fuel plate. Due to this, the large-deformation finite element method is adopted and the Updated Lagrange Method is used. As a result, the second analysis step is divided into several time steps and the configurations of the finite element models are updated after every time step. At every time step, the steady-state temperature field is calculated again; and the structural field is computed subsequently with considering variation of the temperatures with respect to the previous time step.

In ABAQUS, introduction of the irradiation swelling can be implemented by inputting a constant volumetric swelling strain rate of the fuel particle. In the large-deformation finite element analysis, the volumetric swelling strain rate at every time step is corresponding to the updated configuration. As a result, the simulation method is proposed as follows.

The irradiation swelling of the fuel particles at a certain burnup is defined as the relative volumetric change:

$$SW(BU) = \frac{\Delta V}{V_0} \tag{16}$$

where BU denotes burnup (% FIMA), which depicts the ratio of the fissioned atoms to the total fissionable atoms, ΔV is the absolute volumetric change, V_0 is the initial volume.

Firstly, the irradiation swelling at a certain burnup $SW(BU)$ is calculated according to Eqs. (7)–(9), then the relation between the irradiation swelling and the virtual volumetric swelling strain rate is developed as the following.

The total calculation process is divided into n virtual time steps, ensuring that the strain increment and deformation at every step are small. At an arbitrary time step from time t-1 to time t, the ratio of the volume at time t to the volume at time t-1 is set to be constant. That is,

$$\frac{V_t}{V_{t-1}} = \frac{V_{t-1} + \Delta V_t}{V_{t-1}} = 1 + \theta \tag{17}$$

where θ denotes the average volumetric strain induced by the irradiation swelling at every virtual time step. Then

$$\frac{V_n}{V_0} = \frac{V_1}{V_0} \cdot \frac{V_2}{V_1} \cdots \frac{V_n}{V_{n-1}} = (1+\theta)^n \tag{18}$$

$$SW(BU) = \frac{V_n - V_0}{V_0} = (1+\theta)^n - 1 \tag{19}$$

Eq. (19) describes the relationship between the average volumetric strains of every virtual time step and the irradiation swelling at a certain burnup. In order to keep the small strain increment, the total number of the virtual time steps n should be set large enough. In the practical calculation, n is set to a limit value in order that θ tends to be a stable value. Consequently, the average volumetric swelling rate could be introduced

$$\dot{\theta} = \theta / 1 \tag{20}$$

where 1 denotes a virtual time step size.

As a whole, the total computation of the in-pile behaviors is divided into two analysis step: (1) the first analysis step considers only the thermal effects; this analysis step is further divided into several time steps to calculate the thermal–elastoplastic behavior precisely; (2) the second loading step allows for the contribution of the irradiation swelling. And the volumetric swelling strain rate obtained according to Eqs. (16)–(20) is introduced into ABAQUS and enough time steps are divided.

4.2. Validation of the simulation method

The numerical simulation results of the actual volumetric expansions at different burnups are compared with the theoretical

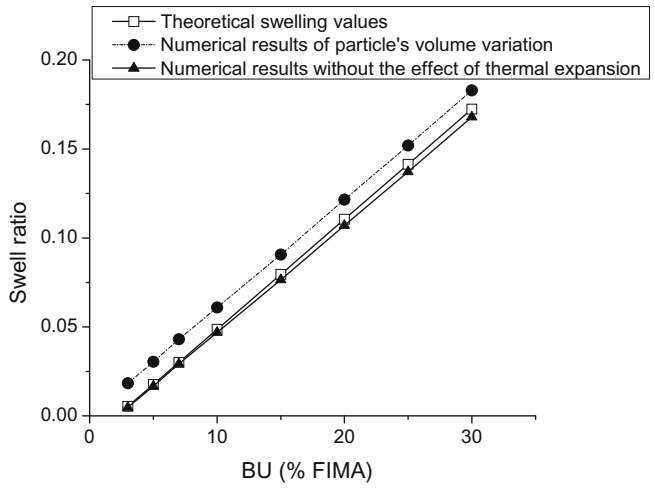

Fig. 4. The comparison of the numerical simulation results of the particle volume expansions with the theoretical ones of irradiation swelling.

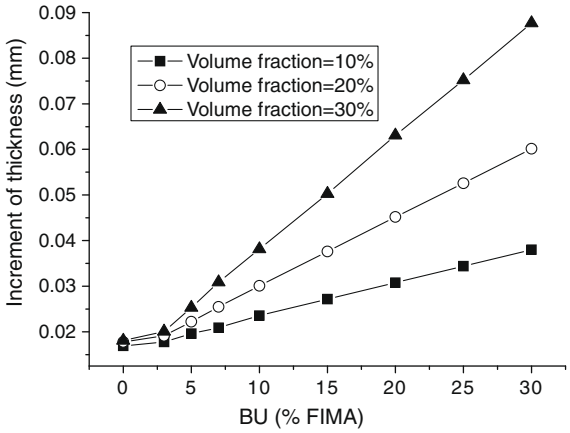

Fig. 5. The plate thickness increments.

ones of the irradiation swelling, as denoted in Fig. 4. It can be discovered that the actual volumetric expansion values are slightly higher than the theoretical computation results of the irradiation swelling; and after eliminating the thermal expansion effect, the obtained volumetric expansion values are very close to and briefly lower than the theoretical ones. This simulation result is reasonable in respect that: (1) the total deformation consists of four parts: the elastic one, the plastic one, the thermal expansion and the irradiation swelling, in which only the elastic deformation, the thermal expansion and the irradiation swelling contribute to the volumetric variation of the fuel particle; (2) the elastic compressive deformation is very small, thus the main contributors of the volumetric variation are the thermal expansion and the irradiation swelling. Therefore, the actual volumetric expansions are higher than the theoretical values of the irradiation swelling; (3) the volumetric expansion results without the effect of the thermal expansion are lower than the theoretical ones of the irradiation swelling and the differences seem to increase with burnup; this is for the reason that: the fuel particles are restrained by the metal matrix around to result in the elastic compressive strains within the fuel particles; and the compressive strains increase with burnup.

Based on the above analysis, it can be obtained that the irradiation-swelling simulation with ABAQUS is validated.

4.3. Plate thickness variations for different particle volume fractions

In order to make sure the security of the dispersion nuclear fuel plate, the plate thickness variations with increasing burnup should be specially considered to prevent the loss-of-coolant accident.

Fig. 5 depicts the increments of the plate thickness, in which the value at zero burnup takes the one induced by the thermal effect at the initial stage of burnup. It is found that for each volume fraction case the plate thickness increments take on a linear relation with burnup after 3% FIMA. The slopes of the lines increase with the particle volume fractions, with the plate thickness increments holding about 38 μm, 60 μm and 88 μm for the three volume fraction cases respectively at 30% FIMA. In fact, the deformation of the fuel plate mainly comes from three contributors: the thermal expansion of the fuel particles, the metal matrix and the cladding, the elastic deformations of the above three components and the particle swelling. Since the temperature variations with increasing burnup because of change of the plate configuration are low for each volume fraction case (found in Fig. 6), it can be assumed that the thermal expansion variations at higher burnups hardly vary; and the contribution of the elastic deformation is also quite small; in the mean time, the irradiation swelling of fuel particles linearly increases with burnup [18]. As a result, the linear variation of the plate thickness with increasing burnup is understandable.

4.4. Temperature variations for different particle volume fractions

Since the irradiation swelling is introduced in the second analysis step which follows the first thermal–elastoplasticity analysis step, the temperature variations with increasing burnup are mainly due to the effect of the configuration change. The calculated maximum temperatures at the fuel plate are depicted in Fig. 6, in which the temperatures at 0% FIMA obtained from the first analysis step and show the results of the steady-state temperature at the initial stage of burnup. The maximum temperature within the fuel plate is at the mid-plane. It can be found out from Fig. 6 that for each volume fraction case the maximum temperatures increase linearly with burnup and at 30% FIMA the maximum values increase only several Kelvins; that means during the second thermal–swelling mechanical analysis the temperature variations with increasing burnup could be neglected. At the same time, from Fig. 6 it can be discovered that the in-pile temperatures increase with the particle volume fractions; and the temperature difference between the 10% and 30% volume fraction cases achieves 50 K, which is big enough to induce relative influence on the strength of both the matrix and the cladding because they are all temperature-dependent. Generally speaking, the strength of metal materials would become weak with rise of the temperature, which means the material strength of the matrix and the cladding decrease with the particle volume fractions, upon which the discussion below is based.

4.5. In-pile mechanical behaviors of the fuel elements

The finite element results at different burnups are obtained for the three cases with different particle volume fractions of the fuel meat. In this section, the effects of the particle volume fractions on the structural fields of dispersion fuel elements are mainly investigated.

4.5.1. Selection of the export paths

The distributions of the Mises stresses, the equivalent plastic strains and the first principle stresses regarding a considered case (particle volume fraction = 20%) at different burnups were presented in Figs. 7–9.

The equivalent plastic strain distributions of the 20% volume fraction case at different burnups are presented in Fig. 7. It can

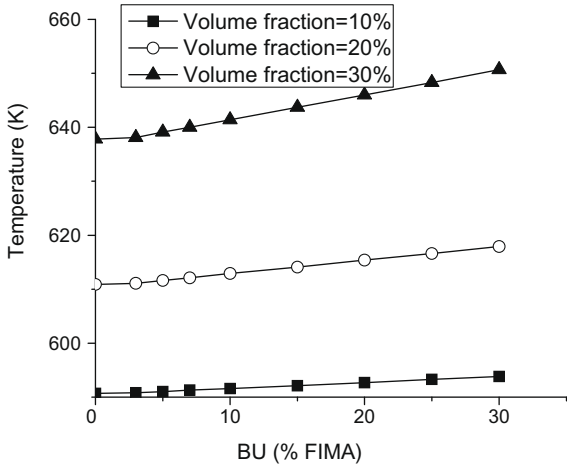

Fig. 6. The variations of the maximum temperatures with increasing burnup.

be found that the largest plastic strains locate at the interfaces between the fuel particles and the matrix; with an increase of burnup, the equivalent plastic strains at the matrix region between two adjacent fuel particles along the thickness direction hardly increase, while those between two adjacent fuel particles along the length or width direction increase obviously.

Similarly, the Mises stress distributions of the 20% volume fraction case at different burnups are illustrated in Fig. 8. It can be found that larger Mises stresses occur at two matrix regions: (1) the interfaces between the fuel particles and the matrix, (2) the matrix between two adjacent fuel particles along the length or width direction; and their values increase with burnup; as for the fuel particles, larger Mises stresses locate near the end points across the thickness direction; and for the cladding, except that the Mises stress values near the interfaces between the fuel meat and the cladding vary with increasing burnup, the Mises stresses at the other regions remain almost the same.

Fig. 9 shows the first principle stress distributions of the 20% volume fraction case at different burnups. It is found that at low burnups the first principle stresses are larger at the matrix regions between two adjacent fuel particles along the thickness direction; however, the first principal stress values at the above regions decrease with burnup and the first principle stresses at the matrix regions between two diagonal fuel particles on the same layer as depicted in Fig. 9b and c increase with burnup and exceed the original maximum values at lower burnups. With rise of burnup, the fast neutrons will attack the matrix continually to harden and embrittle the metal material, thus brittle fracture might be one of the damage forms of the fuel element. As a result, the first principal stress should be taken into account besides the Mises stresses and the equivalent plastic strains.

Based on the above discussion, it is clarified that larger Mises stresses and equivalent plastic strains at the matrix exist at the following regions: the ones at the interfaces between the fuel particles and the matrix and the ones between two adjacent fuel particles along the length or width direction; while the locations with the maximum first principle stresses vary with burnup, and they emerge at the following two regions: the ones between two adjacent fuel particles along the thickness direction or the ones between two diagonal fuel particles on the same layers. The distribution characteristics of the other two cases (the 10% and 30% particle volume fraction cases) are similar to the above one.

Therefore, the following export paths are chosen to describe the in-pile mechanical behaviors and study the effects of the fuel particle volume fractions with increasing burnup, as are displayed in Fig. 10:

(1) *Path* 1: along the semi-circular arcs at the interfaces between the matrix and the fuel particles; the Mises stresses and the equivalent strains are to be exported.

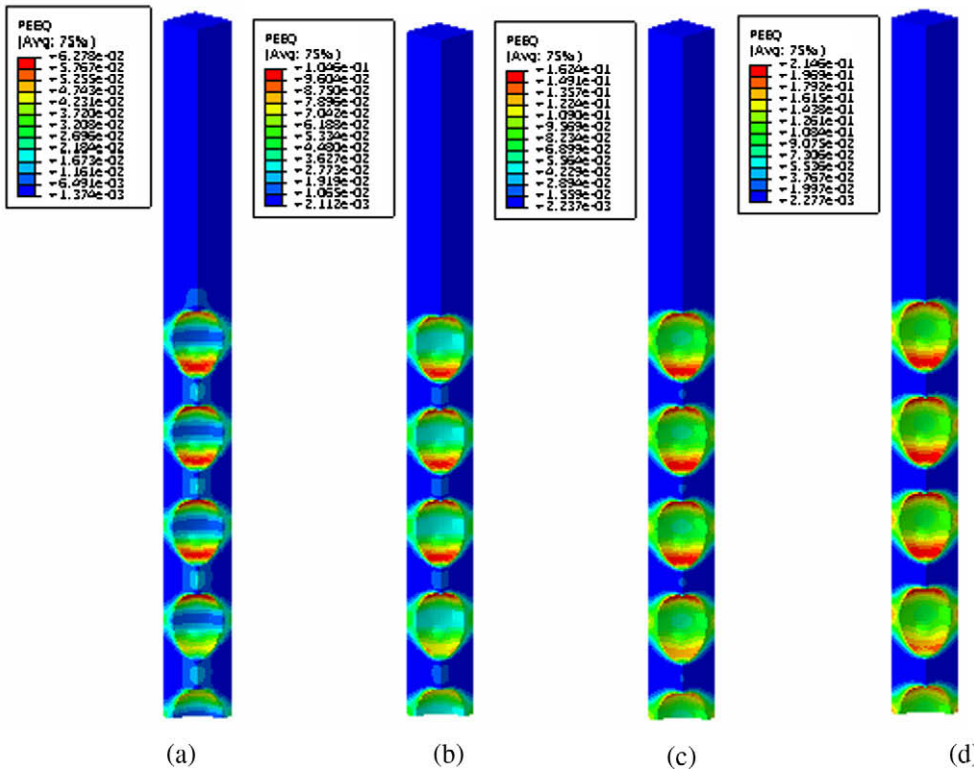

Fig. 7. The equivalent plastic strain distributions of the 20% volume fraction case at different burnups: (a) 5% FIMA, (b) 10% FIMA, (c) 20% FIMA and (d) 30% FIMA.

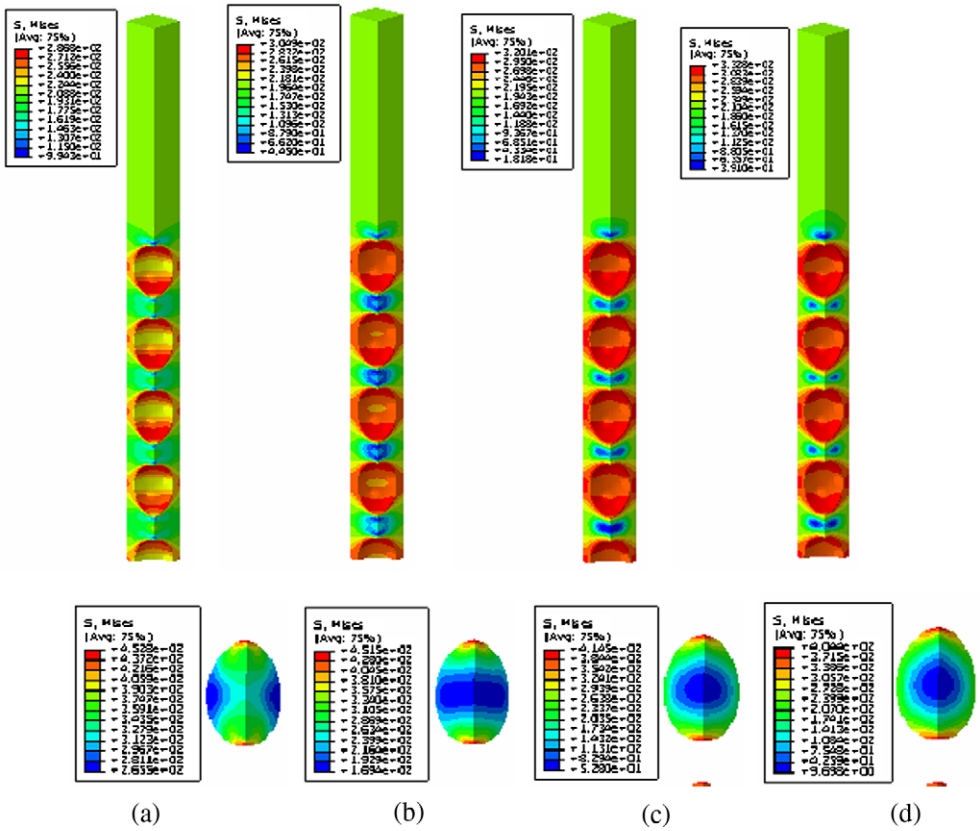

Fig. 8. The Mises stress distributions of the 20% volume fraction case at different burnups: (a) 5% FIMA, (b) 10% FIMA, (c) 20% FIMA and (d) 30% FIMA.

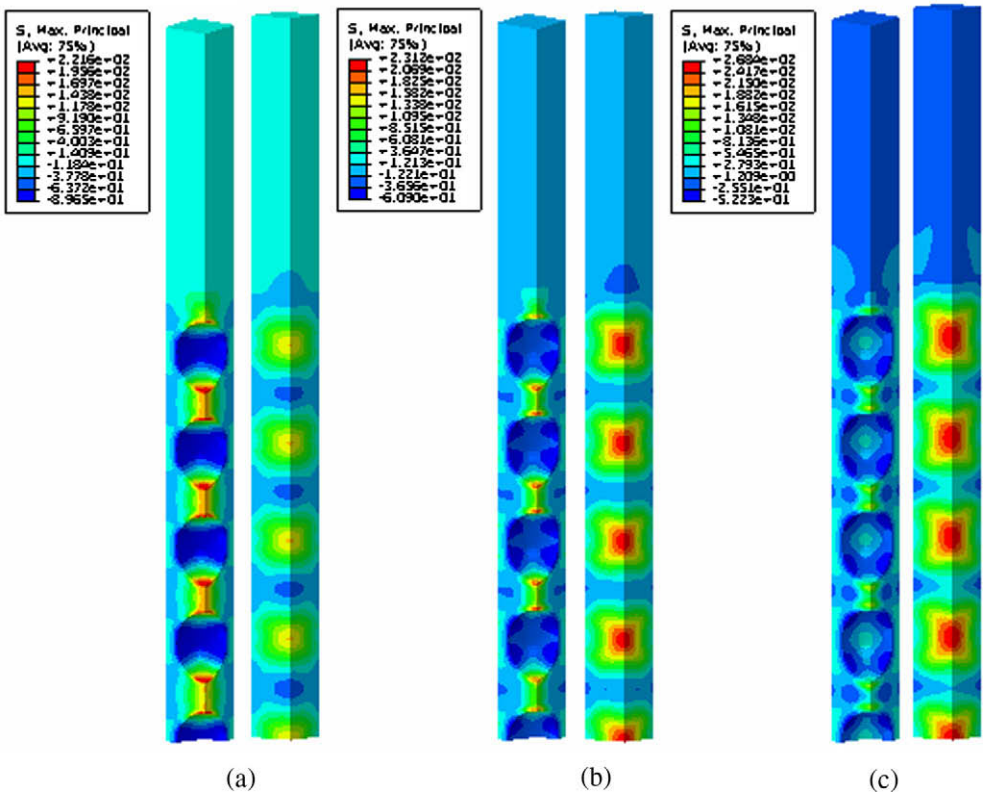

Fig. 9. The first principle stress distributions of the 20% volume fraction case at different burnups: (a) 5% FIMA, (b) 10% FIMA and (c) 20% FIMA.

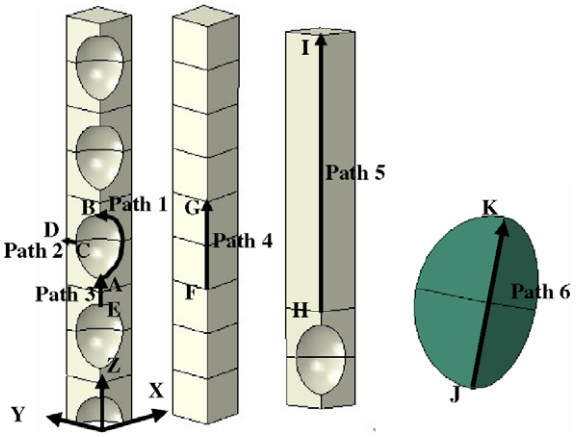

Fig. 10. The export paths of the analysis model.

(2) *Path* 2: along the line between the centers of the two adjacent fuel particles along the width direction; the Mises stresses and the equivalent strains are to be exported.
(3) *Path* 3: along the line between the centers of the two adjacent fuel particles along the thickness direction; the first principle stresses are to be exported.
(4) *Path* 4: along the line at the backside of the fuel particles in the finite element model; the first principle stresses are to be exported.
(5) *Path* 5: along the line from the interface to the outside surface; the Mises stresses, the equivalent strains and the first principal stresses are to be exported.
(6) *Path* 6: along the diameter of the fuel particle along the thickness direction; only the Mises stresses are to be exported.

4.5.2. Effects of the particle volume fractions on the in-pile behaviors of the matrix

4.5.2.1. The Mises stress at the matrix. Fig. 11 illustrates the distributions of the Mises stresses along Path 1 at different burnups. The normalized transverse coordinates are defined as

$$\varsigma = \frac{Z - Z_A}{Z_B - Z_A} \tag{21}$$

where Z_A, Z_B and Z are the z-coordinates of point A, point B and the defined points along Path 1 respectively. It is found that the Mises stress distributions along Path 1 at different burnups almost present the same 'M' shape, with two maximums. The relative low Mises stresses occur at the two ending points and mid-point of Path 1; and the values of the maximums all increase with the particle volume fractions at every burnup. And the Mises stresses at the mid-point decrease with the particle volume fractions. According to the discussion in Section 4.4, the material strength generally decreases with the temperature, thus the 30% volume fraction case is most critical to engender damage with increasing burnup. It can also be observed that the differences of the maximum Mises stresses between the 20% volume fraction case and the 30% volume fraction case are the least.

The distributions of the Mises stresses along Path 2 at different burnups are displayed in Fig. 12, whose normalized transverse coordinates are obtained from

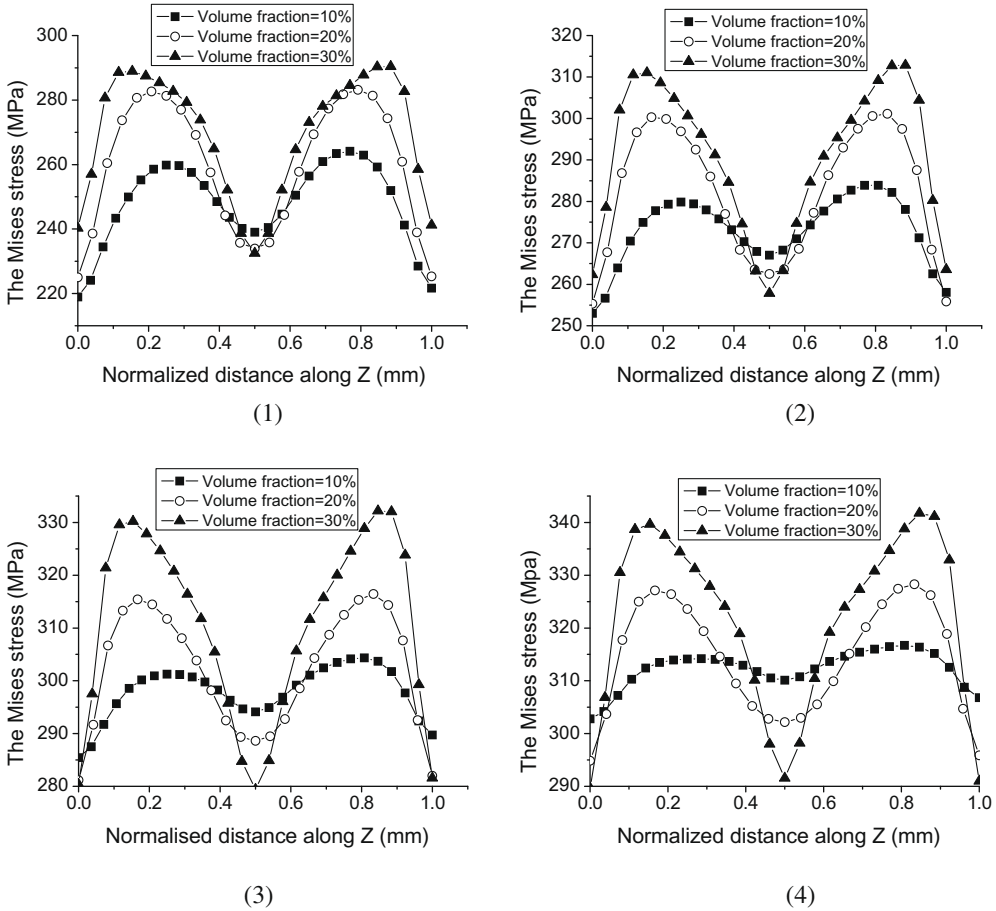

Fig. 11. The distributions of the Mises stresses along Path 1 at different burnups: (1) 5% FIMA, (2) 10% FIMA, (3) 20% FIMA and (4) 30% FIMA.

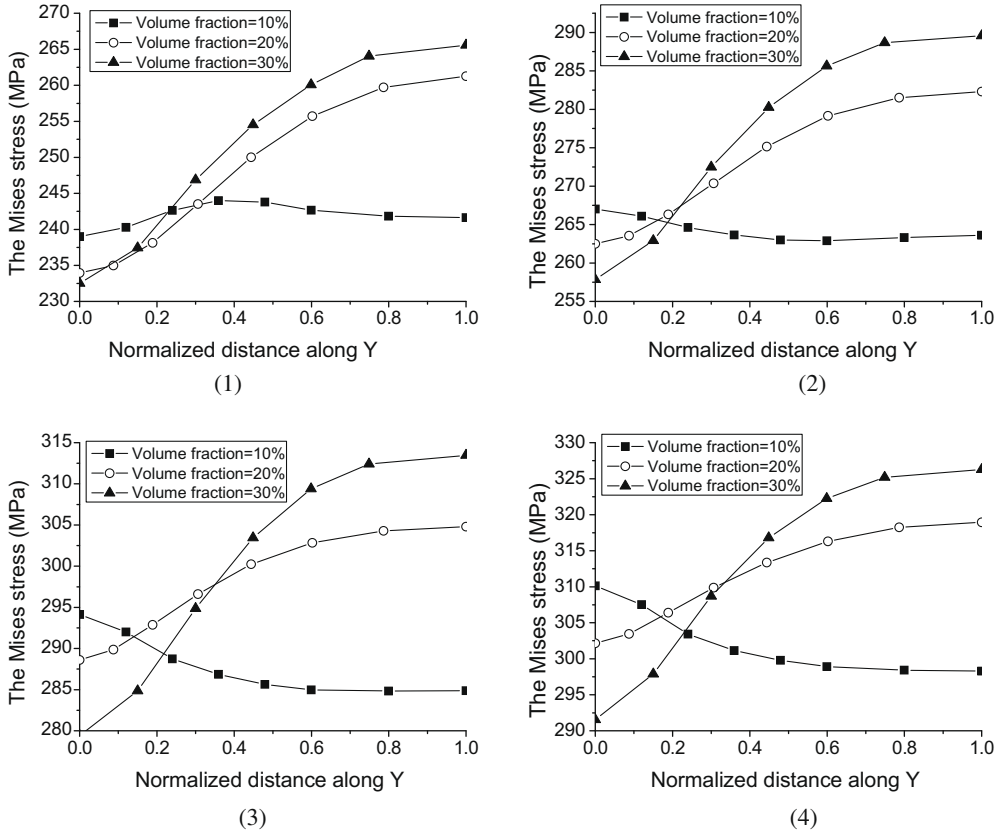

Fig. 12. The distributions of the Mises stresses along Path 2 at different burnups: (1) 5% FIMA, (2) 10% FIMA, (3) 20% FIMA and (4) 30% FIMA.

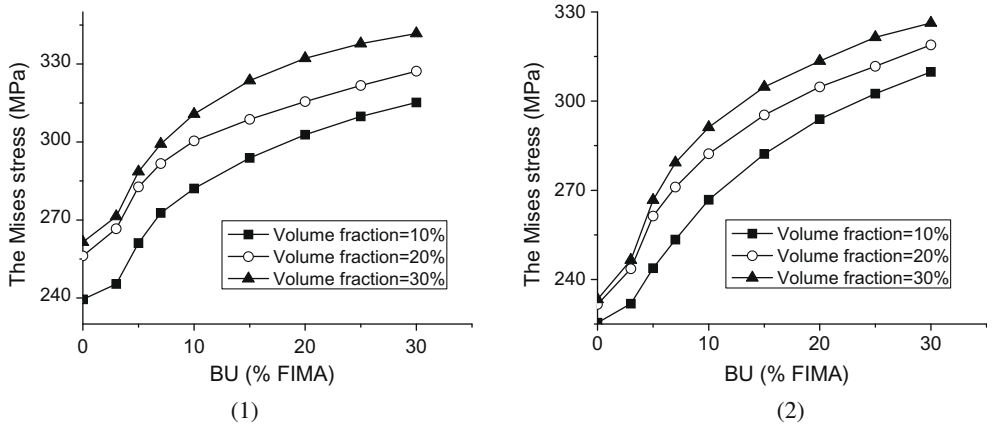

Fig. 13. The maximum Mises stresses at: (1) Path 1 (2) Path 2 for different particle volume fractions with rise of burnup.

$$\varsigma = \frac{Y - Y_C}{Y_D - Y_C} \tag{22}$$

where Y_C, Y_D are Y are the y-coordinates of point C, point D and the defined points along Path 2 respectively. Fig. 12 reveals that the Mises stresses of the 20% and 30% volume fraction cases at different burnups increase along Path 2, whereas the increasing rates decrease with burnup, with the maximums occurring at point D. However, those of the 10% volume fraction case decrease along the path despite the Mises stresses at 5% FIMA. Especially, the maximum Mises stresses at high burnups for the 10% volume fraction case stably present at Point C, which is at the interface between the fuel particle and the matrix; this is for the reason that when the particle volume fractions are lower, the distances between the fuel particles are farther and the mechanical interactions are weaker.

Fig. 13 denotes the maximum Mises stresses at Path 1 and Path 2 for different volume fractions with rise of burnup. Almost the same development trends are presented at Path 1 and Path 2, and the values at Path 1 at each burnup are higher than the ones at Path 2. The maximum Mises stresses for different volume fractions all increase with burnup; the increase rates decrease with burnup as a whole. It can be also observed from Fig. 13 that at the same burnups the maximum Mises stresses at the two paths increase with the particle volume fractions.

4.5.2.2. The equivalent plastic strains at the matrix. Since the deformation-resistance of the plastic material will be weakened if the Mises stresses transcend the yield points, the equivalent plastic strains at the matrix will be also drawn into consideration in this section.

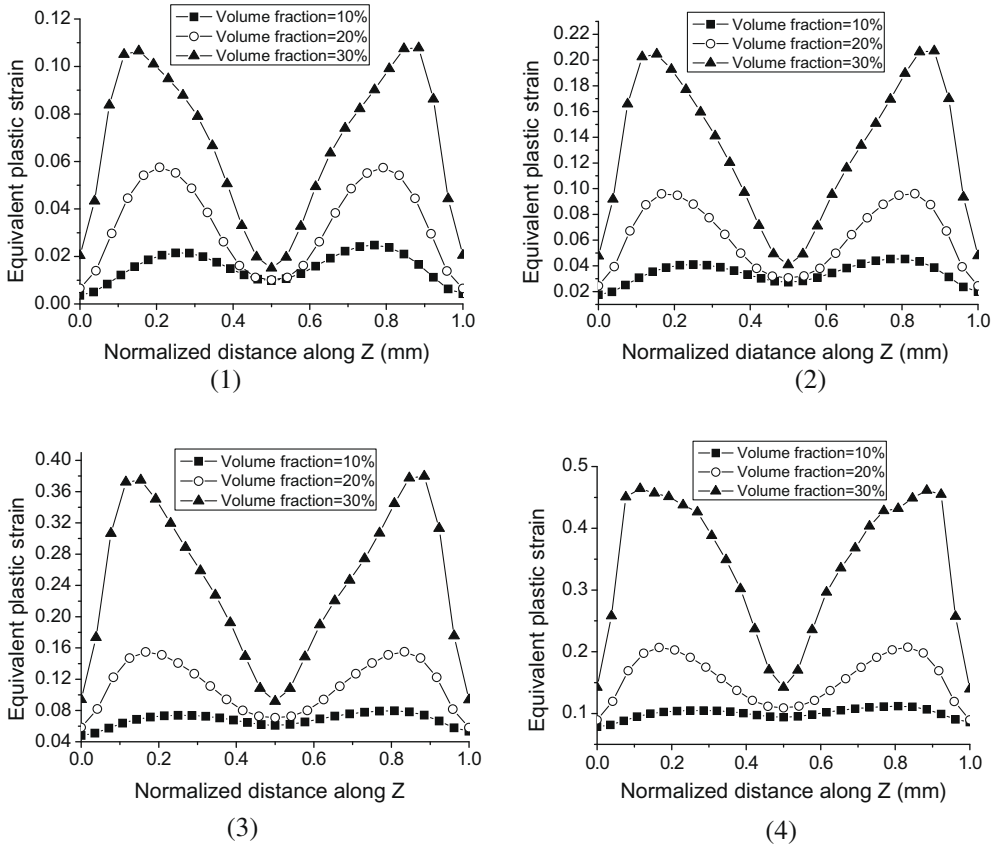

Fig. 14. The distributions of the equivalent plastic strains along Path 1 at different burnups: (1) 5% FIMA, (2) 10% FIMA, (3) 20% FIMA and (4) 30% FIMA.

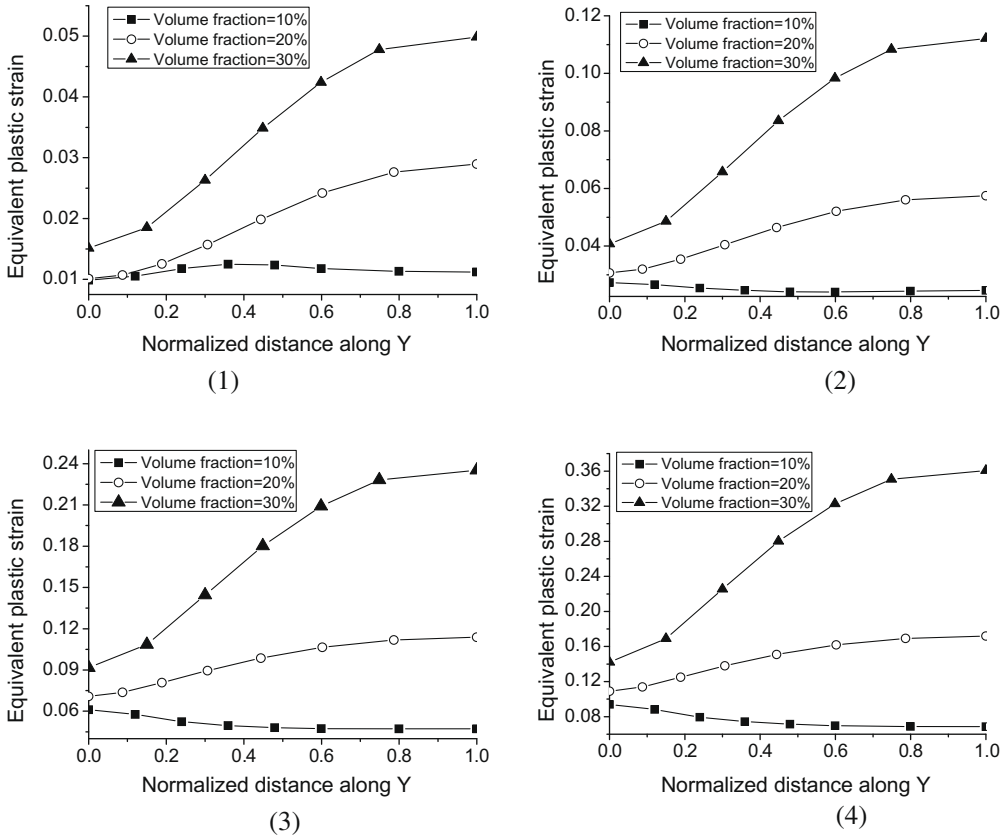

Fig. 15. The distributions of the equivalent plastic strains along Path 2 at different burnups: (1) 5% FIMA, (2) 10% FIMA, (3) 20% FIMA and (4) 30% FIMA.

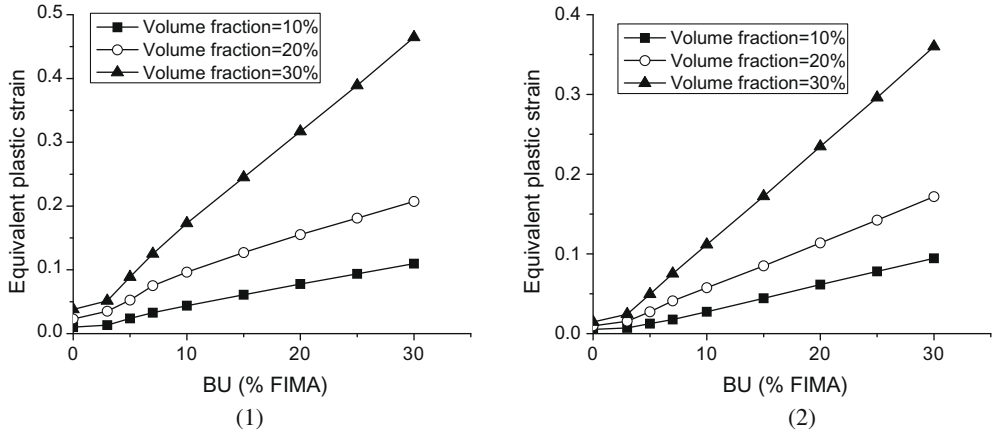

Fig. 16. The maximum equivalent plastic strains at: (1) Path 1 (2) Path 2 for different particle volume fractions with rise of burnup.

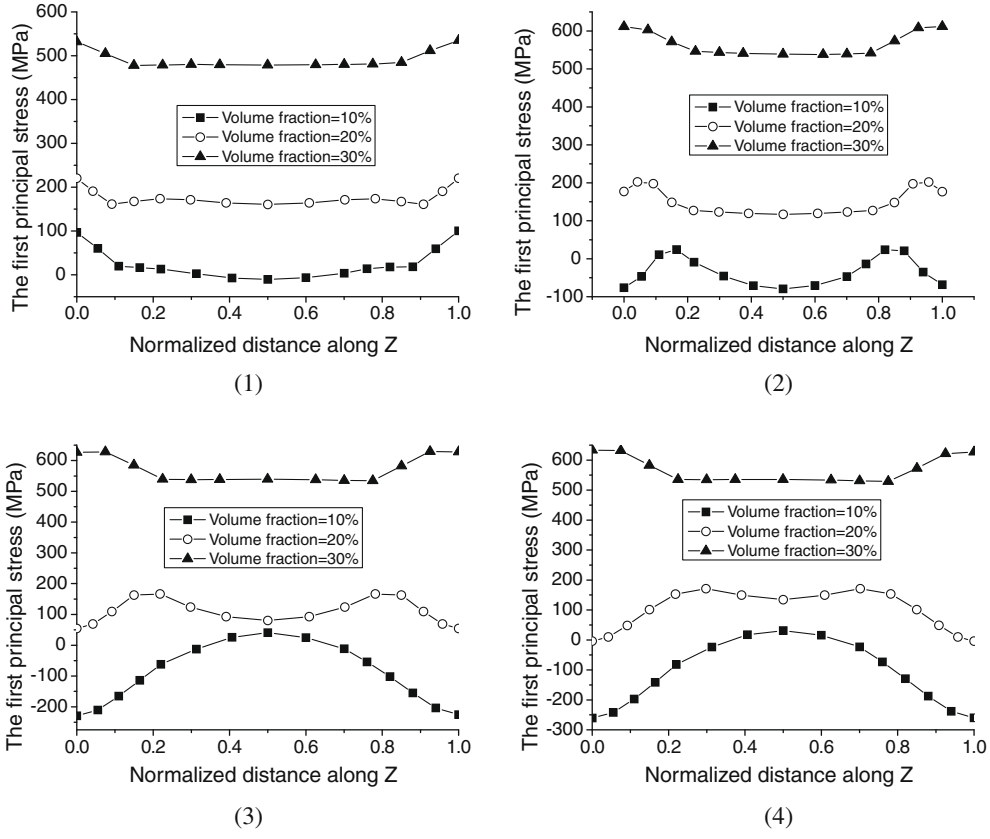

Fig. 17. The distributions of the first principle stresses along Path 3 at different burnups: (1) 5% FIMA, (2) 10% FIMA, (3) 20% FIMA and (4) 30% FIMA.

Fig. 14 depicts the distributions of the equivalent plastic strains along Path 1 at different burnups. It is discovered that the equivalent plastic strains at different burnups present almost the symmetric distribution with respect to the mid-point of Path 1; the maximum values go more and more close to the two end points of this path; and dissimilar to the Mises stresses, the equivalent plastic strains at the mid-point increase with the particle volume fractions, which is for the reason that the plastic material has a lower Mises stress for a certain equivalent plastic strain at higher temperatures and higher temperatures exist at higher particle volume fraction cases; the maximum equivalent plastic strains at Path 1 increase with the particle volume fractions. And it can also be seen that the differences of the maximum equivalent plastic strains between the 30% volume fraction case and the 20% volume fraction case are much larger than those between the 10% volume fraction case and the 20% volume fraction case; combining this result with the relative Mises stress results in Fig. 11, it can be discovered that the ability of deformation-resistance of the plastic material are weaker at higher temperatures.

Fig. 15 illustrates the distributions of the equivalent plastic strain along Path 2 at different burnups, which are also similar to the cases of the Mises stresses in Fig. 12.

The maximum equivalent plastic strains at Path 1 and Path 2 for different particle volume fractions with rise of burnup are displayed in Fig. 16. The relative results at Path 1 and Path 2 almost present the same development trends; higher maximum

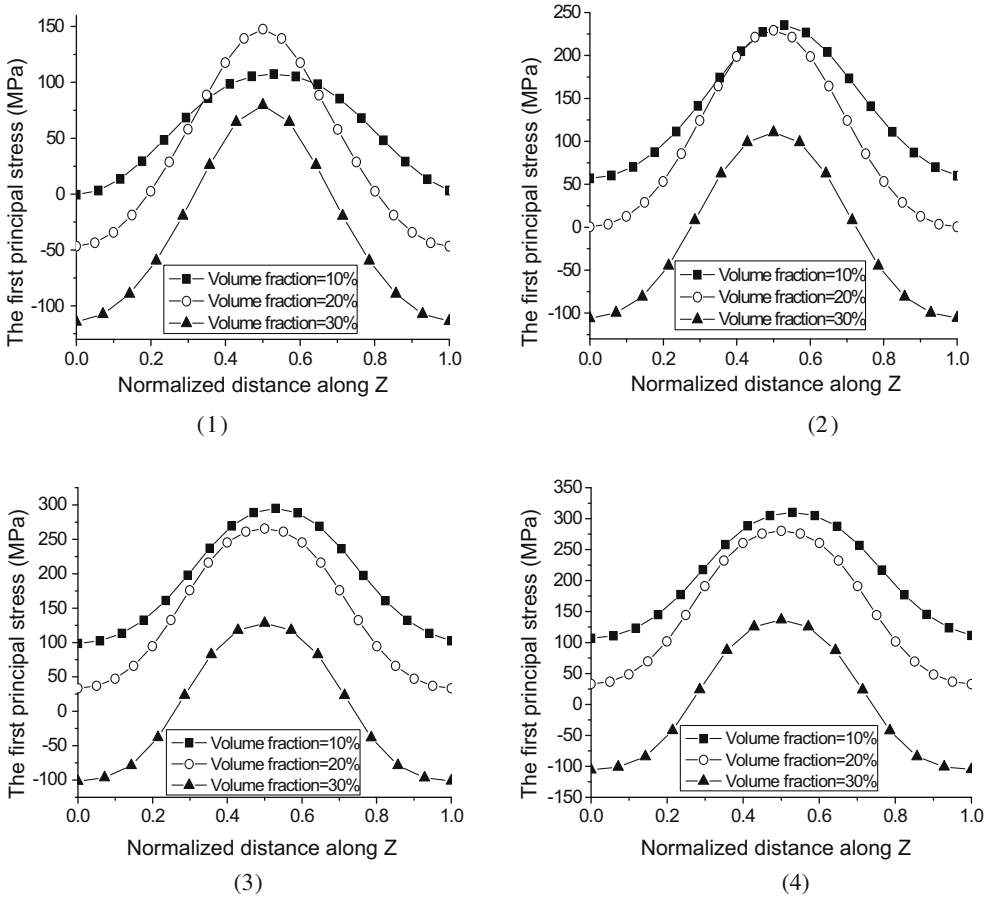

Fig. 18. The distributions of the first principal stresses along Path 4 at different burnups: (1) 5% FIMA, (2) 10% FIMA, (3) 20% FIMA and (4) 30% FIMA.

equivalent plastic strains exist at Path 1. After 5% FIMA, the equivalent plastic strains for different particle volume fractions at both paths increase linearly with burnup; especially, at 30% FIMA, the equivalent plastic strains of the 10% volume fraction case, the 20% volume fraction case and the 30% volume fraction case display 10 times, 9 times and 12 times as large as that induced by the thermal effect respectively. At the same burnups, the maximum equivalent plastic strains increase with the particle volume fractions; and the difference values between 20% volume fraction and 30% volume fraction are higher than those between 10% volume fraction and 20% volume fraction; for instance, as for the values at Path 1 at 30% FIMA, the difference value between 20% volume fraction and 30% volume fraction is 0.257, which is around 2.7 times of that value between 10% volume fraction and 20% volume fraction.

4.5.2.3. The first principal stresses at the matrix. With increasing burnup, brittle fracture might be one of the damage forms of the fuel element, thus the first principal stress should be considered. Figs. 17 and 18 manifest the distributions of the first principal stresses at different burnups along Path 3 and Path 4 respectively. As shown in Fig. 17, the normalized transverse coordinates are defined as

$$\varsigma = \frac{Z - Z_E}{Z_A - Z_E} \tag{23}$$

where Z_A, Z_E are Z are the z-coordinates of point A, point E and the defined points along Path 3 respectively. It can be found from Fig. 17 that the first principal stresses increase with the particle volume fractions at every burnup discussed; at 5% FIMA, the maximum first principal stresses along Path 3 are present at the end points for all the three volume fractions considered; while at the other burnups the locations with the maximum first principal stresses vary with burnup: (1) as for the 10% volume fraction case, two maximums are displayed between the mid-point and the end points when the burnup reaches 10% FIMA, and only one maximum value exists at the mid-point after 20% FIMA; (2) for the 20% volume fraction case, two maximums occur between the mid-point and the end points after 10% FIMA; (3) for the 30% volume fraction case two stable maximums exist very near the two end points of Path 3. And it can be found out that the maximum values of the 10% volume fraction case decrease with burnup; at higher burnups, the compressive stresses almost occupy all the path; the maximum values of the 20% volume fraction case do not vary too much with increasing burnup; and the maximum values of the 30% volume fraction case exceed the other two cases very much and increase with burnup.

As denoted in Fig. 18, the normalized coordinates are defined as

$$\varsigma = \frac{Z - Z_F}{Z_G - Z_F} \tag{24}$$

where Z_F, Z_G and Z are the z-coordinates of point F, point G and the defined point along Path 4 respectively. At every burnup considered, the first principal stresses all increase at first then decrease along Path 4, with the maximums at the mid-points. At 5% FIMA, the largest maximum first principal stress is with the 20% volume fraction case, followed by the 10% volume fraction case and the 30% volume fraction case. Thereafter, however, the maximum first principal stresses decrease with the volume fractions. It can be observed at this path that the maximum values of the 10% volume fraction case increase apparently with burnup and with increasing burnup the maximum values at the total matrix transfer to be at

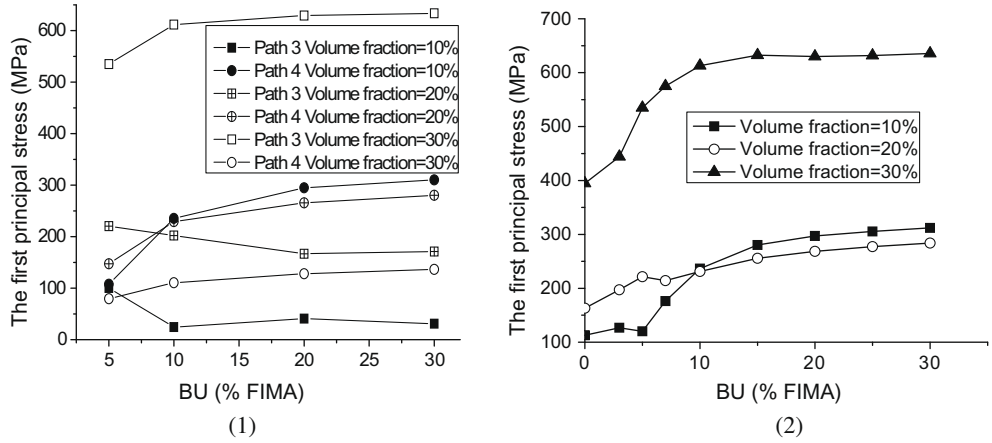

Fig. 19. The maximum first principal stresses: (1) at Path 3 and Path 4 (2) at the matrix for different particle volume fractions with rise of burnup.

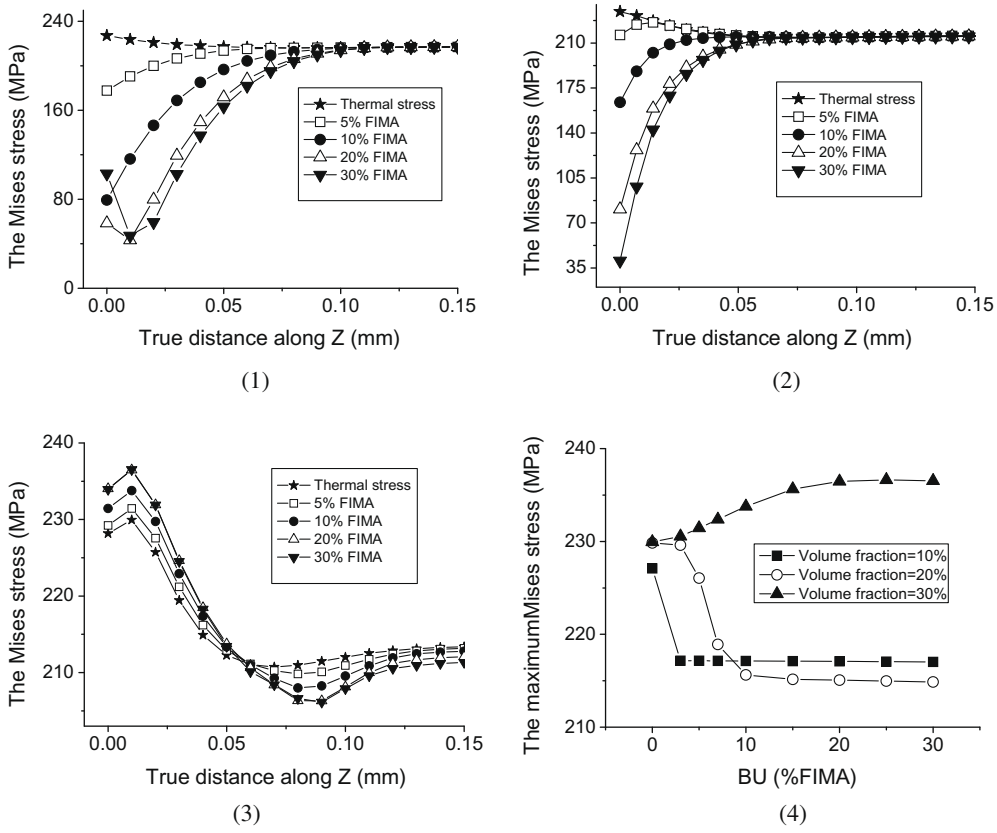

Fig. 20. Effect of variations of the particle volume fractions and burnups on the Mises stresses at the cladding: (1) for the 10% volume fraction case, (2) for the 20% volume fraction case, (3) for the 30% volume fraction case and (4) the maximum Mises stresses for different particle volume fractions.

Path 4; the maximum values of the 20% volume fraction case increase with burnup, and compared with the results at Path 3, it can be obtained that the maximum first principal stresses at the total matrix shift to be at Path 4 at higher burnups; as far as the 30% volume fraction case is concerned, it can be seen that the maximum values at Path 4 are much lower than the ones at Path 3 and the maximum values with increasing burnup always locate at Path 3.

Fig. 19 depicts the maximum first principal stresses at Path 3 and Path 4 together with the maximum ones at the total matrix with rise of burnup. As discussed in Section 4.1, at Path 3 and Path 4 there exist larger first principal stresses, while at different burnups the locations of the maximum first principal stresses might differ. As displayed in Fig. 19(1), the maximum first principal stresses at Path 3 and Path 4 for different volume fractions with rise of burnup are investigated. For the 10% volume fraction case, the maximum first principal stresses at the total matrix occur at Path 4 when the burnup exceeds 5% FIMA. Nevertheless, when the particle volume fraction reaches 20%, the maximum first principal stresses emerge at Path 3 at lower burnups and after 10% FIMA exist at Path 4 instead. Then, as for the 30% volume fraction case, the maximum first principal stresses at Path 3 are even about five times larger than those at Path 4.

Fig. 19(2) illustrates the maximum first principal stresses at the matrix for different volume fractions with rise of burnup. For the

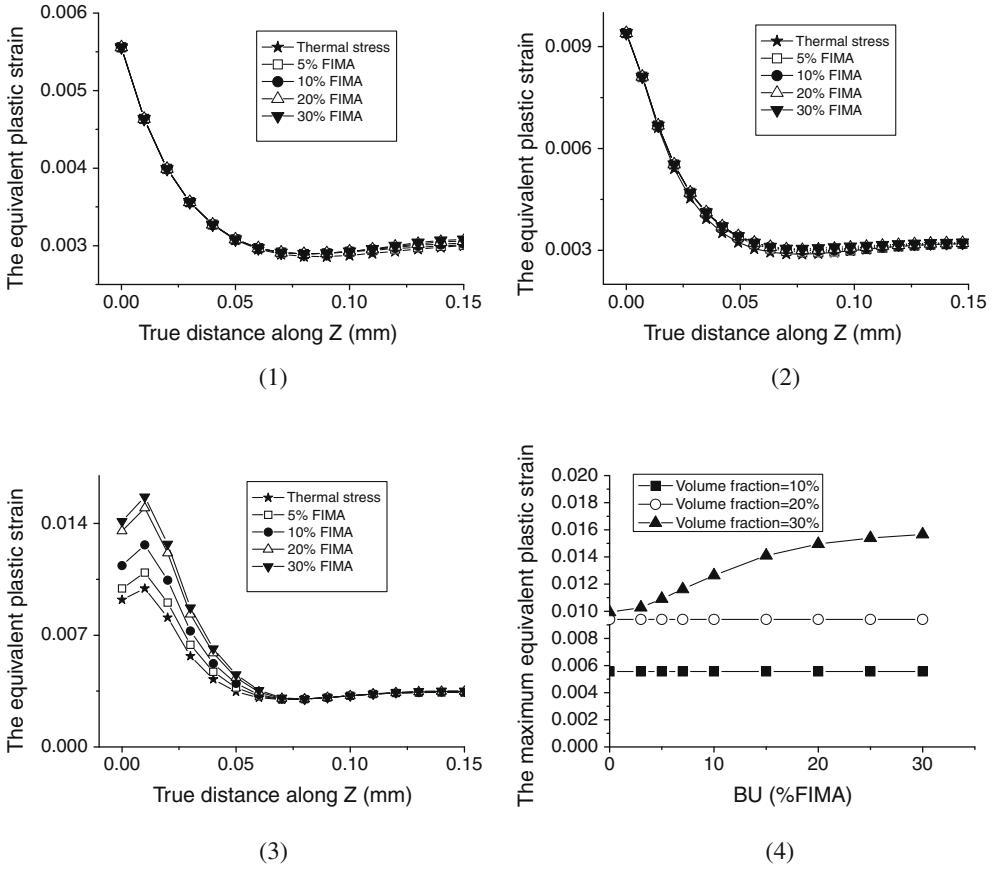

Fig. 21. Effect of variations of the particle volume fractions and burnups on the equivalent plastic strains at the cladding: (1) for the 10% volume fraction case, (2) for the 20% volume fraction case, (3) for the 30% volume fraction case and (4) the maximum equivalent plastic strains for different particle volume fractions.

three volume fraction cases, the maximum first principal stresses increase with burnup, while the increasing rates decrease as a whole as can be found from the slopes of the curves; for instance, as for the 10% volume fraction case, when the burnups are between 5% FIMA and 20% FIMA, the maximum first principal stresses increase about 7 MPa with every 1% FIMA increased; nonetheless, the total increase from 20% FIMA to 30% FIMA is just 6 MPa. The effects of the particle volume fraction vary with burnup: before 10% FIMA, the higher the volume fractions are, the larger the maximum first principal stresses exist; thereafter, the ascending order transforms to be the 20% volume fraction case, the 10% volume fraction case and the 30% volume fraction case. Especially, at 30% FIMA, the maximum first principal stress of the 30% volume fraction case reaches 633 MPa, which is about 2.3 times as large as that of 20% volume fraction case.

4.5.3. Effects of the fuel volume fractions at the cladding

As for the cladding, the distributions of the Mises stresses, the equivalent plastic strains and the first principal stresses are denoted in Figs. 20–22. Since the stresses and strains are almost the same at the region a bit far from the interface between the fuel meat and the cladding, a route with length of only 0.15 mm at Path 5 is chosen as the export path, which could reveal the main variation laws of the mechanical behaviors at the cladding.

4.5.3.1. The Mises stresses at the cladding. Fig. 20 denotes the effect of variation of the volume fractions and burnups on the Mises stresses at the cladding. As displayed in Fig. 20(1), the Mises stress distributions for the 10% volume fraction case at different burnups are presented, in which the true distance along Z is defined by

$$\varsigma = Z - Z_H \tag{25}$$

where Z_H and Z are the z-coordinates of point H and the defined points along Path 5 respectively. And it is chosen that $\varsigma \in [0, 0.15]$mm. At the initial stage of burnup, the maximum Mises stresses occur at the interface between the meat and the cladding, and the Mises stresses decrease along Path 5. However, from 5% FIMA to 20% FIMA the values at the interface decrease and become the minimum along the path. After 20% FIMA, the Mises stresses at point H increase with burnup, with the minimum value occurring near Point H and the maximum values still emerging near the outer surface of the cladding.

rom Fig. 20(2), it can be observed that the locations of the maximum Mises stresses at the cladding for the 20% volume fraction case vary with burnup: (1) under the thermal effect the maximum Mises stress occurs at the interface between the meat and the cladding, and the Mises stresses decrease along Path 5; (2) from 5% FIMA to 10% FIMA, the Mises stresses at Point H (in Fig. 10) decrease with burnup with the maximum values presented near Point H; (3) thereafter, however, the Mises stresses increase along Path 5 and the maximum values exist near the outer surface of the cladding.

Fig. 20(3) reveals the Mises stress distributions for the 30% volume fraction case at different burnups, which presents almost the same variation trend at every burnup. Along Path 5, the Mises stresses increase a little and then decrease sharply, ultimately the stresses increase smoothly toward the outer surface of the cladding. It is found that the maximum Mises stresses increase with burnup, and the stable Mises stresses at the outer surface of the cladding decrease with burnup.

Fig. 20(4) illustrates the maximum Mises stress for different volume fractions with rise of burnup. It is discovered that the max-

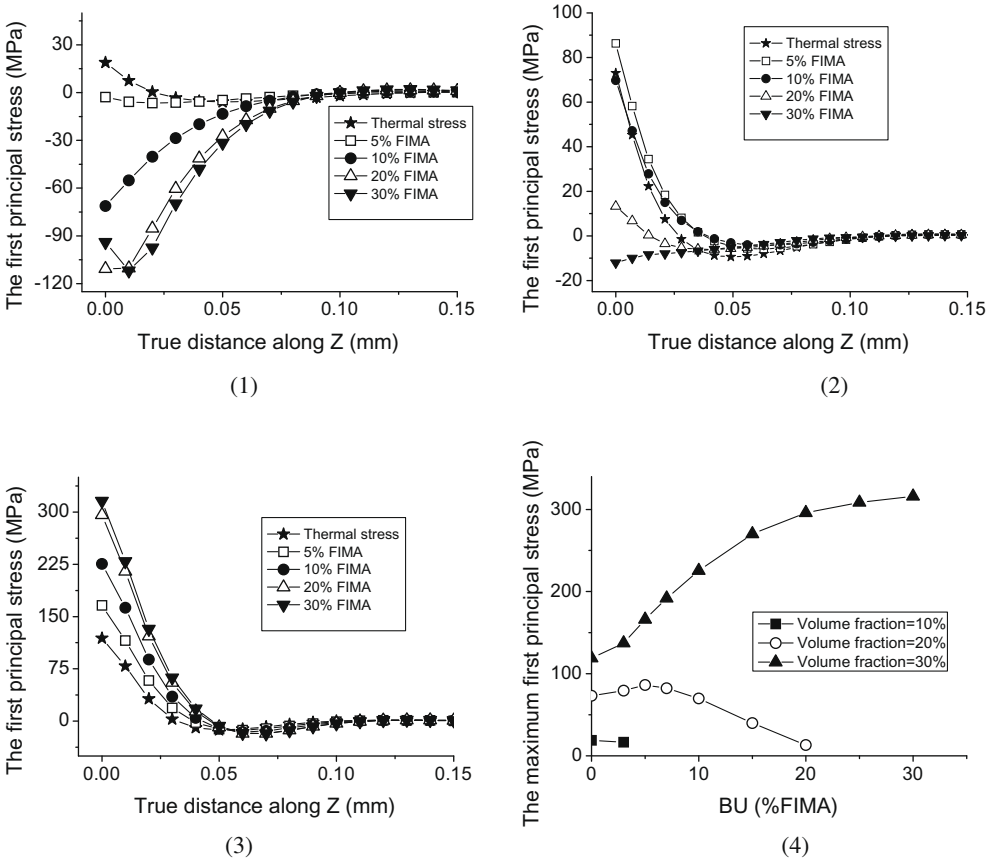

Fig. 22. Effect of variations of the particle volume fractions and burnups on the first principal stresses at the cladding: (1) for the 10% volume fraction case, (2) for the 20% volume fraction case, (3) for the 30% volume fraction case and (4) the maximum first principal stress for different volume fractions.

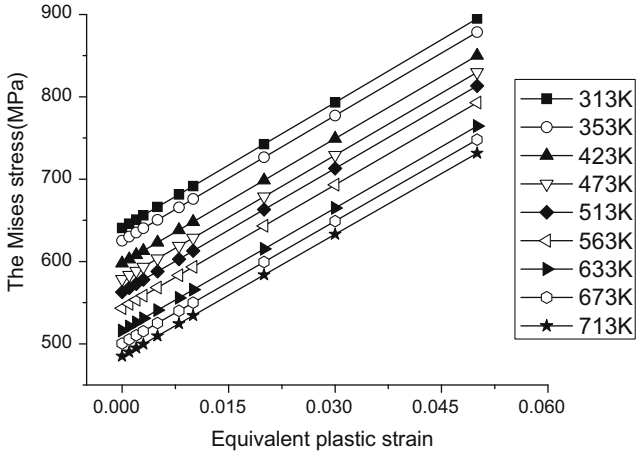

Fig. 23. The Mises yield rule of fuel particles.

imum Mises stresses decrease with burnup for the 10% and 20% volume fraction cases, while they increase with burnup instead for the 30% volume fraction case. Before 10% FIMA, the higher the volume fraction is, the higher the Mises stress is; nevertheless, the ascending order after 10% FIMA transforms to be the 20% volume fraction case, the 10% volume fraction case and the 30% volume fraction case.

4.5.3.2. The equivalent plastic strains at the cladding. Fig. 21 manifests the effect of variations of volume fractions and burnups on the equivalent plastic strains at the cladding. From Fig. 21(1) and (2), it can be observed that for the 10% and 20% volume fraction cases the distribution curves of the equivalent plastic strains along Path 5 at different burnups remain almost overlapped, which means the equivalent plastic strains for the two volume fraction cases are independent of the variations of burnup; and the maximums occur at the interface between the meat and the cladding, this indicates that the plastic strains keep the value induced by the thermal effect and the cladding is in a plastic unloading state with increasing burnup. While as shown in Fig. 21(3), the results for the 30% volume fraction case differ: the maximum values exist near the interface; the higher the burnup is, the larger the equivalent plastic strains are; especially the maximum equivalent plastic strain at 30% FIMA increase by 60% more than that induced by the thermal effect.

Fig. 21(4) depicts the maximum equivalent plastic strains at the cladding for different volume fractions with rise of burnup. It is found that the maximum equivalent plastic strains for the 10% and 20% volume fraction cases remain constant with increasing burnup, while those of the 30% volume fraction case increase with burnup but with a descending rate. At every burnup, the equivalent plastic strains increase with the volume fractions.

4.5.3.3. The first principal stresses at the cladding. Fig. 22 shows the effect of variation of volume fractions and burnups on the first principal stresses along Path 5. The distributions of the first principal stress for the 10% volume fraction case at different burnups are depicted in Fig. 22(1): at lower burnups, the maximum first principal stresses locate at the interface between the meat and the cladding; however, after 5% FIMA, only compressive principal stresses are observed, thus there is no possibility to crack because of the effect of the tensile stress. As for the 20% volume fraction case

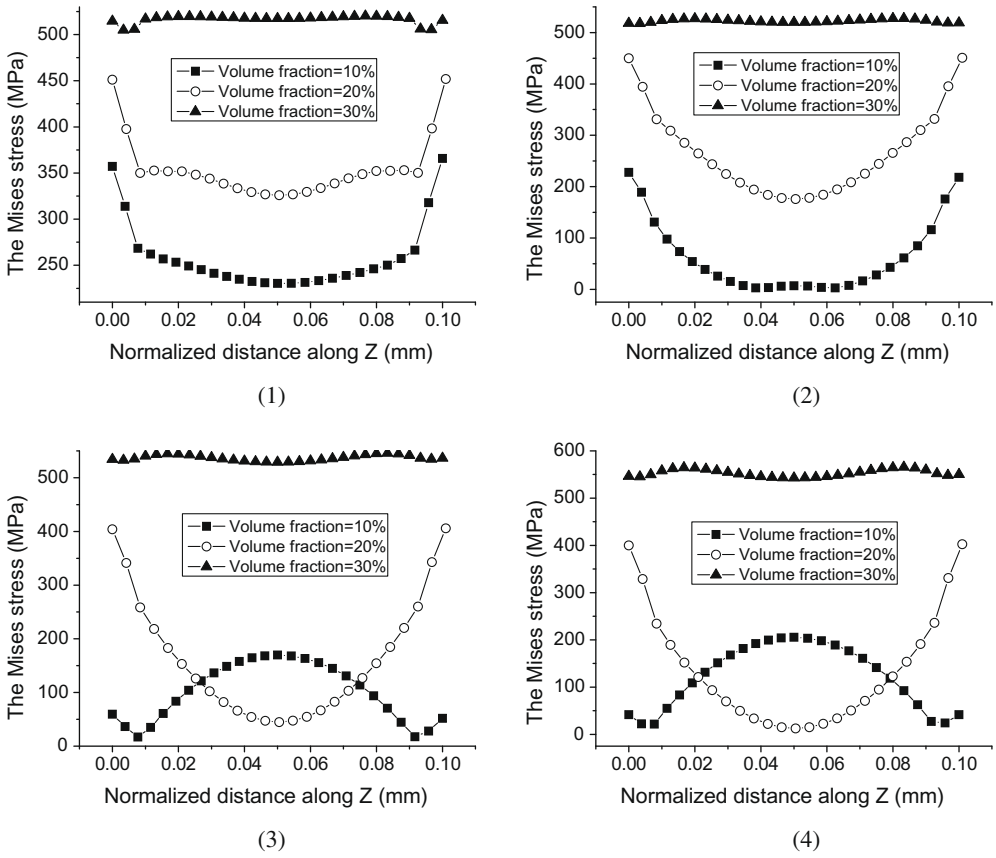

Fig. 24. The distribution of the Mises stresses along Path 6 at different burnups: (1) 5% FIMA, (2) 10% FIMA, (3) 20% FIMA and (4) 30% FIMA.

displayed in Fig. 22(2), before 20% FIMA, the maximum tensile principal stresses emerge at the interface between the meat and the cladding, and the values first increase until 5% FIMA and then decrease with burnup; nevertheless, at 30% FIMA, no tensile principal stress is presented at Path 5. When the particle volume fraction reaches 30% as shown in Fig. 22(3), the maximum tensile principal stresses at the interface increase with burnup to achieve a very large value at 30% FIMA.

The maximum first principal stresses for different particle volume fractions along Path 5 are displayed in Fig. 22(4), which reveals the different variation trends with burnup for different volume fractions. As for the 10% volume fraction case, the tensile principal stresses are presented only before 3% FIMA, with 18 MPa as the maximum; whereas the 20% volume fraction case occupies a wider range of burnup with existence of tensile principal stresses: before 20% FIMA, the maximum tensile principal stresses increase first and then decrease with burnup, with 89 MPa at 5% FIMA as the maximum. For the 30% volume fraction case, the maximum tensile principal stresses increase with burnup, despite with a descending increasing rate, with the maximum of 316 MPa at 30% FIMA.

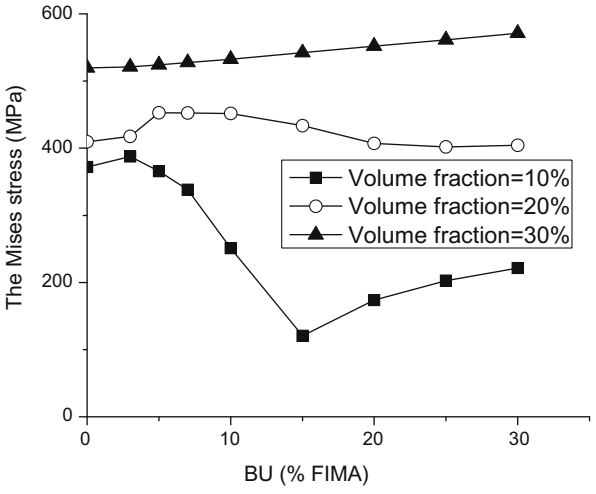

Fig. 25. The maximum Mises stress at Path 6 for different particle volume fractions with rise of burnup.

4.5.4. Effects of the particle volume fractions on the in-pile mechanical behaviors of fuel particles

The calculated results indicate that no plastic strain is presented at the fuel particles for the 10% and 20% volume fraction cases, and for the 30% volume fraction case the maximum equivalent plastic strain at the fuel particles is only 0.0113, which is much lower than that at the matrix. In fact, according to Eq. (7), the Mises yielding rule of fuel particles is obtained and displayed in Fig. 23. As calculated in thermal analysis, the maximum temperatures at the fuel particles for the 10%, 20% and 30% volume fraction cases are 594 K, 613 K and 651 K respectively. Under thermal effect, the maximum Mises stresses for each volume fraction case are 371.9 MPa, 411.4 MPa and 542.8 MPa. As a result, it is understandable that no plastic deformation is presented for the former two cases but the plastic deformation exists for the latter one with considering the fuel swelling.

The distributions of the Mises stresses along Path 6 at different burnups are shown in Fig. 24, where the normalized coordinates are denoted by

$$\varsigma = \frac{Z - Z_J}{Z_K - Z_J} \tag{26}$$

where Z_J, Z_K are Z are the z-coordinates of point J, point K and the defined points along Path 6 respectively. As for the 10% volume fraction case, the maximum Mises stresses occur at the two end points of Paht 6 respectively at 5% FIMA and 10% FIMA, whereas they exist at the mid-point respectively at 20% FIMA and 30%FIMA. However, the distributions of the Mises stresses along Path 6 for the 20% and 30% volume fraction cases almost stay invariable: the Mises stresses of the 20% volume fraction case decrease first then increase along the path with the maximum values locating at the end points, and those of the 30% volume fraction case are nearly constant along the path.

Fig. 25 denotes the maximum Mises stress at Path 6 with increasing burnup for different particle volume fraction cases. It indicates that with increasing burnup the maximum Mises stresses for the 10% volume fraction case increase first, decrease subsequently and then increase smoothly at higher burnups; the largest value occurs at 3% FIMA and the lowest one exists at 15% FIMA. As for the 20% volume fraction case, the Mises stresses increase first and then decrease with burnup, with the maximum value being at 5% FIMA. However, for the 30% volume fraction case the maximum Mises stresses increase monotonously with rise of burnup. Especially, when the burnup reaches 30% FIMA, compared to the maximum Mises stresses induced by the thermal effect, the one for the 10% volume fraction case is 150 MPa lower, and the one for the 20% volume fraction case is 5 MPa lower, while the one for the 30% volume fraction case is 51 MPa higher. It might be inferred that the main factors to affect the mechanical behaviors at the fuel particles could be the complex interaction between the particles and the matrix.

5. Conclusion

In this study, the total burnup is divided into two stages: the initial stage of burnup and the increasing stage of burnup. The thermal–mechanical behaviors at the initial stage of burnup are mainly induced by the temperature differences between the steady-state temperature field and the room temperature. And the in-pile mechanical behaviors at the increasing stage of burnup result from the particle swelling with increasing burnup. Thus, simulations of the irradiation-induced mechanical behaviors of dispersion nuclear fuel elements in ABAQUS are divided into two analysis steps, and every analysis step contains a number of time steps. A method of modeling the particle swelling in a large-deformation elastoplastic analysis is proposed. Through comparing the numerical simulation results of the particle swelling with the theoretical ones, the proposed method is validated. The finite element models for different particle volume fraction cases are developed respectively and the effects of the particle volume fractions on the in-pile mechanical behaviors are investigated. The following conclusions can be obtained within the considered parameters in this study:

For the matrix of the fuel meat,

(1) Larger Mises stresses at the matrix of the fuel meat occur at two kinds of regions with increasing burnup: (1) the interfaces between the matrix and the fuel particles; (2) and the locations between the two adjacent fuel particles along the length or width direction. Within the range of the investigated burnups, the maximum Mises stresses at the matrix increase with burnup for each volume fraction case considered, and the increase velocities decrease with burnup as a whole. At each burnup, the maximum Mises stresses at the matrix also increase with rise of the particle volume fractions.
(2) The maximum equivalent plastic strains at the matrix exist at the interfaces between the matrix and the fuel particles. For the three volume fraction cases discussed, the maximum equivalent plastic strains at the matrix increase with burnup; especially, they increase almost linearly with burnup after the initial stage. At each burnup, the maximum equivalent plastic strains at the matrix also increase with the particle volume fractions.
(3) With increasing burnup, for the 10% volume fraction and 20% volume fraction cases, the locations of the maximum first principal stresses shift to the regions between the two diagonal fuel particles on the same layer perpendicular to the thickness direction; and the ones of the 30% volume fraction case remain at the regions between the two adjacent particles along the thickness direction. At low burnups, the larger the volume fractions are, the larger the maximum first principal stresses are; while at high burnups, the 20% volume fraction case holds the lowest value.
(4) The thickness increments of plate-type dispersion nuclear fuel elements increase nearly linearly with the particle volume fractions at every burnup investigated.

For the cladding,

(1) At low burnups, the maximum Mises stresses increase with burnup; while at high burnups, the ascending order transforms to be the cases of 20% volume fraction, 10% volume fraction and 30% volume fraction.
(2) The maximum equivalent plastic strains at the cladding locate at the interface between the meat and the cladding or near this interface. For the 10% and 20% volume fraction cases, the distribution of the equivalent plastic strains at the cladding does not change with burnup; while the values increase with burnup for the 30% volume fraction case. At each burnup, the maximum equivalent plastic strains increase with the particle volume fractions.
(3) For the 10% and 20% volume fraction cases, the maximum first principal stresses decrease with burnup, while they increase with burnup instead for the 30% volume fraction case. For the 10% volume fraction case, the maximum tensile stresses only exist at the burnups lower than 5% FIMA; while for the cases with higher particle volume fractions, the maximum tensile stresses occupy a larger range of burnup; and the larger the volume fractions are, the larger the tensile principal stresses exist.

For the fuel particles,

(1) At each burnup, the higher the volume fractions are, the larger the maximum Mises stresses exist. The locations of the maximum Mise stresses vary with variations of the burnup and the particle volume fractions.
(2) For the 10% and 20% volume fraction cases, the fuel particles are still in an elastic state at the considered burnups; whereas the plastic strains have occurred at the 30% volume fraction case.

Acknowledgements

The authors thank for the supports of the Natural Science Foundation of China (10772049, 10672042), Research and Development Program of China (863 Program, 2009AA04Z408), the Natural Science Foundation of Shanghai (06ZR14009), the Pujiang Scholar Program, and the Wangdao Scholar Program (08076) of Fudan University.

References

[1] V.P. Sinha, G.J. Prasad, P.V. Hegde, R. Keswani, C.B. Basak, S. Pal, G.P. Mishra, Journal of Alloys and Compounds 473 (2009) 238–244.
[2] Lee Van Duyn. Evaluation of the Mechanical Behavior of a Metal-matrix Dispersion Fuel for Plutonium Burning, Georgia Institute of Technology: A Thesis for the Degree Master of Science in Mechanical Engineering, 2003.
[3] F. Huet, V. Marelle, J. Noirot, P. Sacristan, P. Lemoine, in: Proceedings of the 2003 International Meeting on Reduced Enrichment for Research and Test Reactors, Chicago, IL, 5–10 October 2003.
[4] H.J. Ryu, Y.S. Han, J.M. Park, S.D. Park, C.K. Kim, Journal of Nuclear Materials 321 (2003) 210.
[5] A. Leenaers, S. Van den Berghe, E. Koonen, et al., Journal of Nuclear Materials 335 (2004) 39.
[6] F. Huet, J. Noirot, V. Marelle, S. Dubois, P. Boulcourt, P. Sacristan, S. Naury, P. Lemoine, in: Proceedings of the Ninth International Topical Meeting on Research Reactor Fuel Management, Budapest, Hungary, 10–13 April 2005.
[7] Chan Bock Lee, Yong Sik Yang, Dae Ho Kim, Sun Ki Kim, Je Geun Bang, Journal of Nuclear Science and Technology 45 (1) (2008) 60–71.
[8] S.J. Oh, K.H. Kim, S.J. Jang, D.B. Lee, Y.S. Lee, J.M. Park, H.D. Park, C.K. Kim, The development of U-7WT. %Mo for Large Particle Powers by Centrifugal Atomization, RRFM2006 Transactions, Session 2: Poster Fuel Development, pp. 136–140.
[9] J.L. Snelgrove, G.L. Hofman, M.K. Meyer, C.L. Trybus, T.C. Wiencek, Nuclear Engineering and Design 178 (1997) 119–126.
[10] H. Taboada, J. Rest, M.V. Moscarda, M. Markiewicz, E. Estevez, in: Proceedings of the 24th International Management on Reduced Enrichment for Research and Test Reactors, San Carlos de Bariloche, Argentina, 3–8 November 2002.
[11] J. Rest, The DART Dispersion Analysis Research Tool: A Mechanistic Model for Predicting Fission-Product-Induced Swelling of Aluminum Dispersion Fuels, ANL-95/36, 1995.
[12] S.L. Hayes, M.K. Meyer, G.L. Hofman, J.L. Snelgrove, R.A. Brazener, in: Proceedings of the 2003 International Meeting on Reduced Enrichment for Research and Test Reactors, Chicago, IL, 5–10 October 2003.
[13] S.L. Hayes, G.L. Hofman, M.K. Meyer, J. Rest, J.L. Snelgrove, in: 2002 International Meeting on Reduced Enrichment for Research and Test Reactors, Bariloche, Argentina, 3–8 November 2002.
[14] V. Marelle, S. Dubois, M. Ripert, J. Noirot, P. Lemoine, in: The RERTR-2007 International Meeting on Reduced Enrichment for Research and Test Reactors, 23–27 September, Diplomat Hotel – Prague, Prague, Czech Republic, 2007.
[15] V. Marelle, F. Huet, P. Lemoine, in: Proceedings of the Eighth International Topical Meeting on Research Reactor Fuel Management, München, Germany, 21–24 March 2004.
[16] Roberto Saliba, Horacio Taboada, Ma. Virginia Moscarda, in: 2003 International Meeting on Reduced Enrichment for Research and Test Reactors, Chicago, IL, 5–10 October 2003.
[17] K. Böning, W. Petry, Journal of Nuclear Materials 383 (2009) 254–263.
[18] Shurong Ding a, Xin Jiang, Yongzhong Huo, Lin an Li, Journal of Nuclear Materials 374 (2008) 453–460.
[19] Shurong Ding, Yongzhong Huo, XiaoQing Yan, Modeling of the heat transfer performance of plate-type dispersion nuclear fuel elements, Journal of Nuclear Materials (2009), doi:10.1016/j.jnucmat.2009.04.015.
[20] P.G. Lucuta, H.S. Matzke, I.J. Hastings, Journal of Nuclear Materials 232 (1996) 166–180.
[21] MATPRO-09, A Handbook of Materials Properties for Use in the Analysis of Light Water Reactor Fuel Rod Behavior, USNRC TREE NUREG-1005, 1976.
[22] W. Chubb, V.W. Storhok, D.L. Keller, Nuclear Technology 18 (1973) 231–255.
[23] T. Nakajima, M. Ichikawa, et al., FEMAXI-III: A Computer Code for the Analysis of Thermal and Mechanical Behaior of Fuel Rods, AERI-1298, 1985.
[24] W. Wiesenack, M. Vankeerberghen, R. Thankappan, Assessment of UO2 Conductivity Degradation based on In-pile Temperature Data, HWR-469, 1996.
[25] E.F. Fisher, C.J. Renken, Physical Review 45 (1954) A482–A494.
[26] D.L. Hagrman, G.A. Reyman, MATPRO-Version11, A Handbook of Materials Properties for Use in the Analysis of Light Water Reactor Fuel Rod Behavior, NUREG/CR-0497, TREE-1280, Rev. 3 (1979) A.